

SCIENTIFIC REPORTS

OPEN

Fabrication of Epitaxial Fe_3O_4 Film on a Si(111) Substrate

Nozomi Takahashi¹, Teodor Huminiuc², Yuta Yamamoto¹, Takashi Yanase³, Toshihiro Shimada³, Atsufumi Hirohata⁴ & Taro Nagahama³

Received: 21 April 2017

Accepted: 22 June 2017

Published online: 1 August 2017

The application of magnetic oxides in spintronics has recently attracted much attention. The epitaxial growth of magnetic oxide on Si could be the first step of new functional spintronics devices with semiconductors. However, epitaxial spinel ferrite films are generally grown on oxide substrates, not on semiconductors. To combine oxide spintronics and semiconductor technology, we fabricated Fe_3O_4 films through epitaxial growth on a Si(111) substrate by inserting a $\gamma\text{-Al}_2\text{O}_3$ buffer layer. Both of $\gamma\text{-Al}_2\text{O}_3$ and Fe_3O_4 layer grew epitaxially on Si and the films exhibited the magnetic and electronic properties as same as bulk. Furthermore, we also found the buffer layer dependence of crystal structure of Fe_3O_4 by X-ray diffraction and high-resolution transmission electron microscope. The Fe_3O_4 films on an amorphous- Al_2O_3 buffer layer grown at room temperature grew uniaxially in the (111) orientation and had a textured structure in the plane. When Fe_3O_4 was deposited on Si(111) directly, the poly-crystal Fe_3O_4 films were obtained due to SiO_x on Si substrate. The epitaxial Fe_3O_4 layer on Si substrates enable us the integration of highly functional spintronic devices with Si technology.

In the field of spintronics, spin injection and transport phenomena have attracted much attention owing to the possibility of producing novel functional devices^{1–3}. In particular, the combination of spintronics and semiconductors is a promising technology for the development of the next stage of spintronic devices, e.g., spin-FET or logic devices^{4,5}. The spin injection technique, in which the spin-polarized currents are injected from ferromagnetic metals into conventional semiconductor materials^{2,3,6}, has been intensely investigated for the preparation of spintronic devices. As a result, researchers have succeeded in nonlocal detection⁷ or the observation of the Hanle effect¹, which demonstrates the spin state in the semiconductor; thus, the behavior of the spin current in the semiconductor can be determined⁸. Recently, graphene has also been the subject of spin injection because the spin diffusion length in such light elements is expected to be long owing to small spin-orbit interaction^{9,10}.

The source of the spin current plays an important role in obtaining high-efficiency spin injection. Magnetic oxides are one of the most promising spin source candidates. However, ferromagnetic metals have been used so far because of convenience during fabrication. Magnetic oxides possess unique properties^{11–14}; Fe_3O_4 or (LaSr) MnO_3 have a half-metallic state, which provides highly spin polarized current¹⁵, and NiFe_2O_4 or CoFe_2O_4 are magnetic insulators, which means that they could work as a spin filter tunnel barrier^{16–18}. $\gamma\text{-Fe}_2\text{O}_3$ is another candidate as the spin filter barrier. It is the spinel type ferrimagnetic insulator that is obtained by over oxidation of Fe_3O_4 ¹⁹. Recently, NiCo_2O_4 with spinel structure was discovered to exhibit large magnetoresistance effects²⁰. Therefore, the combination of magnetic oxides and semiconductors enables us to produce new functional devices. Some research groups fabricated the magnetic oxide on oxide semiconductor, Nb:SrTiO₃, and investigated the transport characteristics including spin transport of the junctions^{19,21}. However, epitaxial growth of magnetic oxide on Si, which is the most important semiconductor, has not been established because the surface of Si is easily oxidized by the oxygen atmosphere during the evaporation of the magnetic oxides²².

In this study, we grew Fe_3O_4 epitaxially on a Si(111) substrate by the insertion of an ultrathin $\gamma\text{-Al}_2\text{O}_3$ buffer layer. Fe_3O_4 is the ferrimagnetic conducting oxide with spinel crystal structure. At 120K, Fe_3O_4 shows phase transition called Verwey transition, at which the electric resistivity increases drastically and the crystal symmetry decreases from face-centered cubic to monoclinic^{23–25}. Fe_3O_4 is expected to be half-metallic theoretically, meaning to have a spin polarization of 100%¹⁵, and a spin polarization of more than 80% was observed experimentally using a spin-resolved photoemission spectroscopy²⁶. An ultrathin $\gamma\text{-Al}_2\text{O}_3$ layer was inserted to prevent surface

¹Graduate School of Chemical Sciences and Engineering, Hokkaido University, Sapporo, 060-8628, Japan.

²Department of Physics, University of York, Heslington, York, YO10 5DD, England. ³Graduate School of Engineering, Hokkaido University, Sapporo, 060-8628, Japan. ⁴Department of Electronic Engineering, University of York, Heslington, York, YO10 5DD, England. Correspondence and requests for materials should be addressed to T.N. (email: nagahama@eng.hokudai.ac.jp)

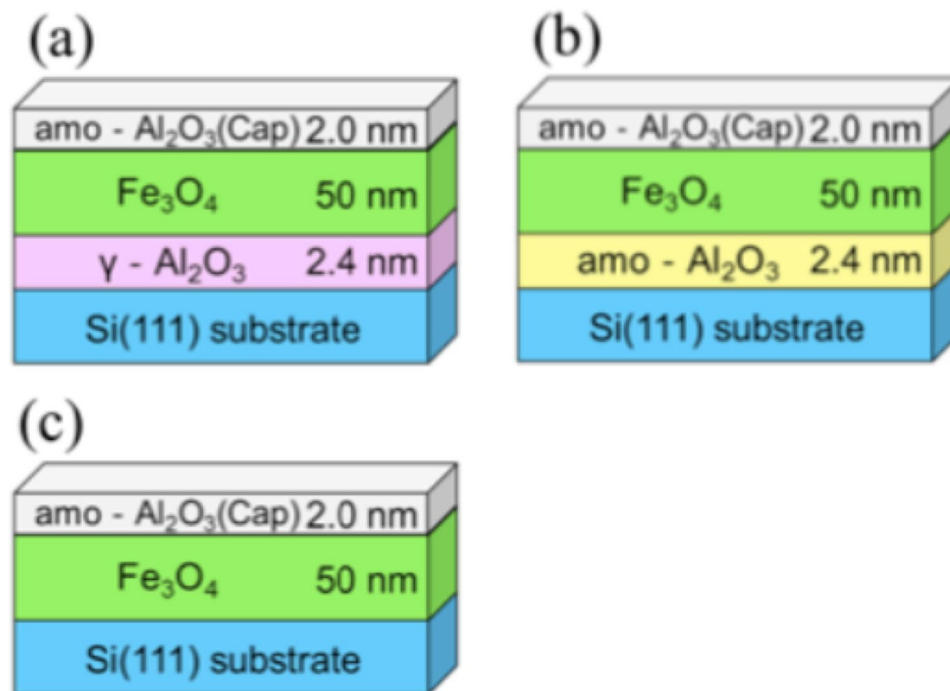


Figure 1. Sample structures: (a) the sample with γ -Al₂O₃ buffer layer (EPI), (b) with amorphous-Al₂O₃ buffer layer (AMO), and (c) without a buffer layer (W/O).

oxidation of Si during the Fe₃O₄ growth. γ -Al₂O₃ is an aluminum oxide with the same spinel structure as Fe₃O₄ and the lattice constant of γ -Al₂O₃ is 7.91 Å, which is three halves of that of Si with lattice mismatch of -2.9% ²⁷. From the viewpoint of the crystal structure, Fe₃O₄ and γ -Al₂O₃ seems to grow on Si epitaxially.

γ -Al₂O₃ (111) epitaxial growth on Si(111) was reported by two research groups recently. Jung *et al.* formed a γ -Al₂O₃ (111) layer by annealing an Al layer on protective Si oxide, which was carefully oxidized to be reduced by the Al layer²⁸. Merckling *et al.* fabricated γ -Al₂O₃ (111) by the deposition of an Al₂O₃ source under ultra-high vacuum²⁹. In the former method, it is difficult to optimize the oxidation of the Si layer and the thickness of Al film. In contrast, the latter method is simple if an ultra-high vacuum system is accessible.

In this study, the epitaxial γ -Al₂O₃ buffer layers were prepared using an ultra-high vacuum system and the Fe₃O₄ layer was fabricated by reactive molecular beam epitaxy. We investigated the crystal structure, magnetic and electric properties of the Fe₃O₄ layer on Si(111) with an epitaxial γ -Al₂O₃ buffer layer, an amorphous-Al₂O₃ buffer layer, and without a buffer layer. We succeeded in the fabrication of high quality Fe₃O₄ films on Si(111) substrates. The buffer layer had a significant effect on the crystal structure of the Fe₃O₄ layers.

Results and Discussion

Epitaxial growth. The γ -Al₂O₃ and Fe₃O₄ layers were grown by molecular beam epitaxy method. The structures of the samples were (a) Si(111)/ γ -Al₂O₃ 2.4 nm/Fe₃O₄ 50 nm/amorphous-Al₂O₃ 2.0 nm, (b) Si(111)/amorphous-Al₂O₃ 2.4 nm/Fe₃O₄ 50 nm/amorphous-Al₂O₃ 2.0 nm and (c) Si(111)/Fe₃O₄ 50 nm/amorphous-Al₂O₃ 2.0 nm, as shown in Fig. 1 (hereafter referred to as (a) EPI, (b) AMO and (c) W/O), respectively. After treatment of the Si substrate, we confirmed that the *in-situ* reflection high energy electron diffraction (RHEED) pattern of the Si substrate had a (7 × 7) streak pattern (Supplementary Fig. S1). This means that the surface of Si was clean and flat. Figure 2(a) and (b) show the RHEED pattern of γ -Al₂O₃ and Fe₃O₄ in EPI. The direction of the incident electron beam was [11-2]. The RHEED patterns of γ -Al₂O₃ and Fe₃O₄ were clear streak patterns indicating that γ -Al₂O₃ and Fe₃O₄ grew epitaxially. Therefore, the γ -Al₂O₃ film was considered to play a role of a buffer layer for epitaxial growth of Fe₃O₄. The surface roughness of γ -Al₂O₃ and Fe₃O₄ were estimated to be very small in value by atomic force microscope (AFM) (shown in Supplementary Fig. S2).

Figure 2(c) and (d) show the RHEED pattern of amorphous-Al₂O₃ and Fe₃O₄ in AMO. The amorphous-Al₂O₃ layer was deposited at room temperature. After the deposition of Al₂O₃, as shown in Fig. 2(c), the Si (7 × 7) streak pattern turned into a halo pattern, which indicated that the Al₂O₃ layer was amorphous. Figure 2(d) shows the RHEED pattern of Fe₃O₄ on the amorphous-Al₂O₃. A ring and streak pattern was observed, which implied the presence of a polycrystalline surface. Thus, the epitaxial γ -Al₂O₃ played a crucial role in the formation of epitaxial Fe₃O₄ on the Si substrate.

Figure 2(e) and (f) show the RHEED pattern of the Si substrate and Fe₃O₄ in W/O. The surface of the Si substrate exhibited a diffused streak pattern owing to the introduction of oxygen gas, which oxidized the Si surface. In Fig. 2(f), the RHEED pattern of Fe₃O₄ on SiO_x shows a halo pattern, which indicated that spinel-type Fe₃O₄ was not formed.

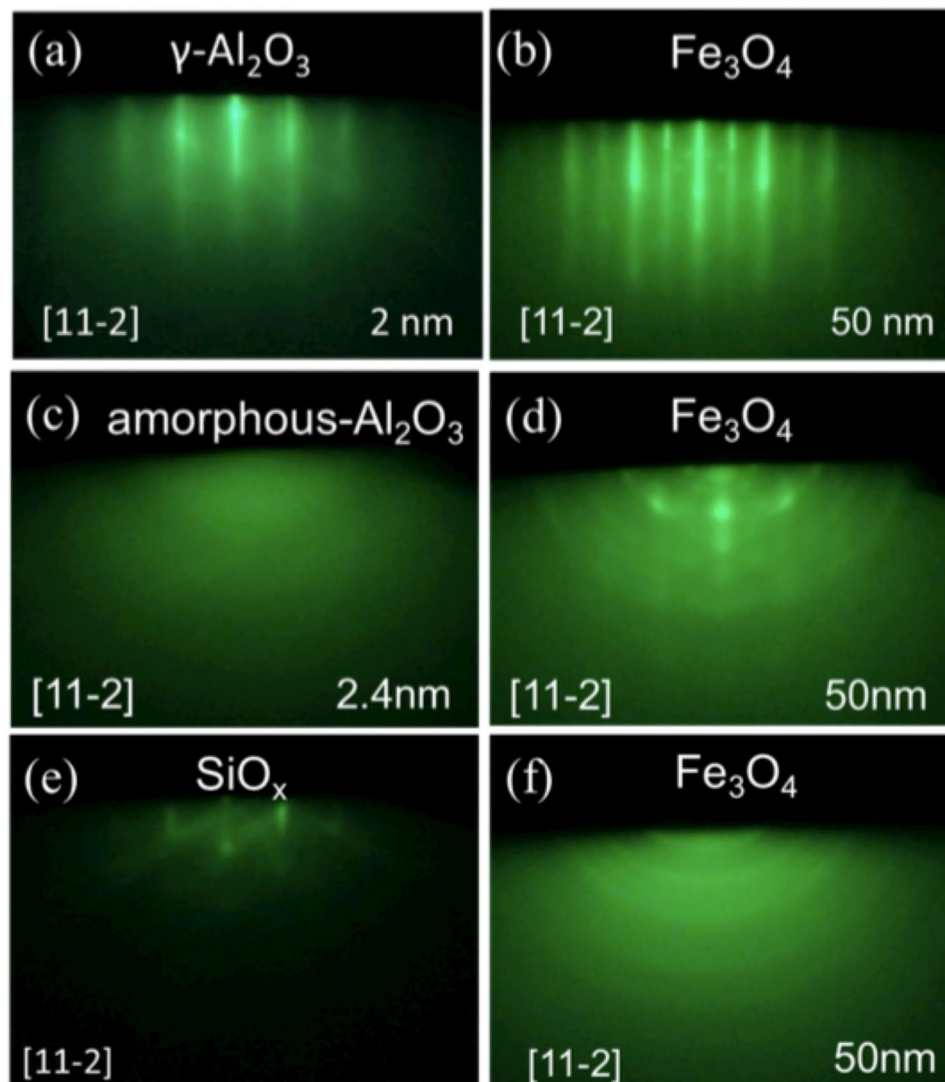


Figure 2. RHEED patterns: (a) γ - Al_2O_3 and (b) Fe_3O_4 film on γ - Al_2O_3 in EPI, (c) amorphous- Al_2O_3 and (d) Fe_3O_4 on amorphous- Al_2O_3 in AMO, (e) Si surface before depositing Fe_3O_4 , and (f) Fe_3O_4 on Si substrate in W/O.

X-ray diffraction. To confirm the crystallization, the θ - 2θ X-ray diffraction (XRD) measurements were carried out on three samples, as shown in Fig. 3(a). The diffraction pattern of Fe_3O_4 on an γ - Al_2O_3 buffer layer in EPI (red line) exhibited four peaks (18.3° , 37.2° , 57.2° , 79.4°), which were in agreement with the diffraction patterns of Fe_3O_4 (111), (222), (333) and (444) planes. This indicated that the Fe_3O_4 film was (111)-oriented without other orientations or phases. The lattice constant measured by XRD was estimated to be 8.39 \AA . The lattice constant of the in-plane direction was estimated to be 8.23 \AA (Supplementary Fig. S3), which is smaller than the bulk lattice parameter. Therefore, the Fe_3O_4 was considered to be compressed in-plane.

To investigate the in-plane epitaxial relationship, we conducted ϕ -scan measurements of Si(311) and Fe_3O_4 (4-40), as shown in Fig. 3(b). The six peaks of Fe_3O_4 (4-40) appeared at 60° intervals, indicating the presence of two 180° rotated domains in the Fe_3O_4 layer. The epitaxial relationships were $[11-2]\text{Fe}_3\text{O}_4(111)$ and $[-1-12]\text{Fe}_3\text{O}_4(111)$ parallel to $[11-2]\text{Si}(111)$, as exhibited in Fig. 3(c). In addition, the peaks of the Fe_3O_4 film were broader than that of the Si substrate. There was a lattice mismatch of 5.7% at γ - $\text{Al}_2\text{O}_3/\text{Fe}_3\text{O}_4$.

The θ - 2θ XRD diffraction pattern of Fe_3O_4 in AMO (blue line) exhibited four peaks, which was identical with the diffraction pattern of Fe_3O_4 in EPI. Therefore, the Fe_3O_4 in AMO was also (111)-oriented. However, the RHEED pattern in Fig. 1(d) implied the presence of a polycrystalline structure. Furthermore, the $\text{Fe}_3\text{O}_4(4-40)$ diffraction peak was not observed in the ϕ -scan measurement. Therefore, we concluded that the Fe_3O_4 had a textured structure and the growth direction was (111).

The θ - 2θ XRD diffraction pattern of Fe_3O_4 in W/O (green line) exhibited small peaks related to $\text{Fe}_3\text{O}_4(311)$, (400), (422) and unknown peaks. In a previous study³⁰, the XRD of Fe_3O_4 on SiO_2 indicated that the Fe_3O_4 layer was polycrystalline and contained other phases.

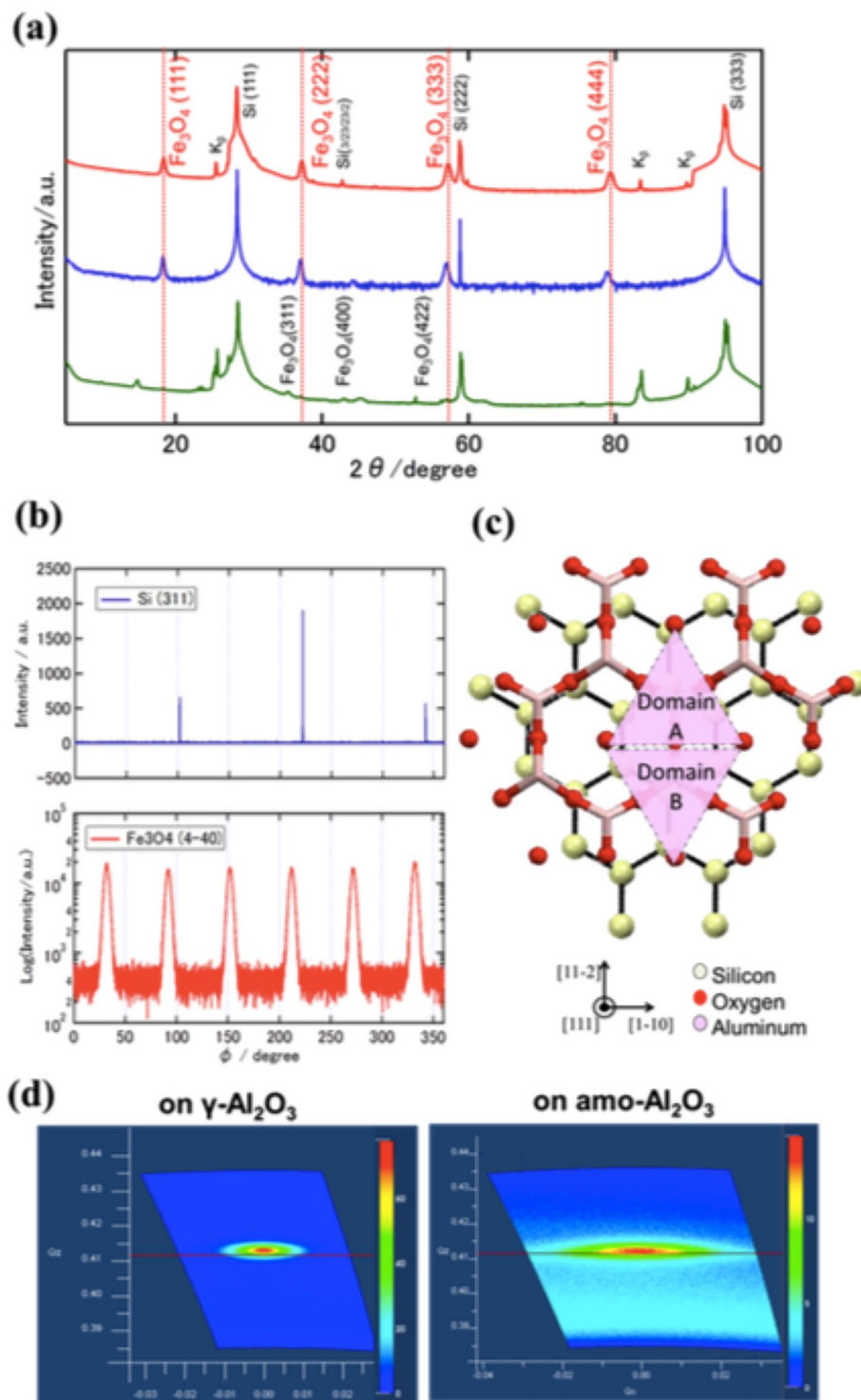


Figure 3. X-Ray diffraction: (a) θ - 2θ XRD profiles, (b) ϕ -scan measurement, (c) Epitaxial relationship between Si and $\gamma\text{-Al}_2\text{O}_3$, (d) X-ray reciprocal space maps of Fe_3O_4 on $\gamma\text{-Al}_2\text{O}_3$ in EPI and Fe_3O_4 on amorphous- Al_2O_3 in AMO.

To investigate the crystallinity of the Fe_3O_4 layer in detail, we carried out X-ray reciprocal space mapping around the symmetric (222) diffraction for Fe_3O_4 in EPI and AMO (Fig. 3(d)). The symmetrical scan showed that the Fe_3O_4 (222) spot on amorphous- Al_2O_3 was larger than the Fe_3O_4 spot on $\gamma\text{-Al}_2\text{O}_3$, which means that the Fe_3O_4 in AMO had an angle distribution in the growth directions. Although the reason for the (111) oriented Fe_3O_4 growth on amorphous- Al_2O_3 /Si(111) was unclear, two possibilities exist that could explain this growth. The first is a reduction in the total anisotropy energy related to the surface energy and interface energy³¹. The difference between AMO and W/O could be attributed to the difference of the surface and interface energy of amorphous- Al_2O_3

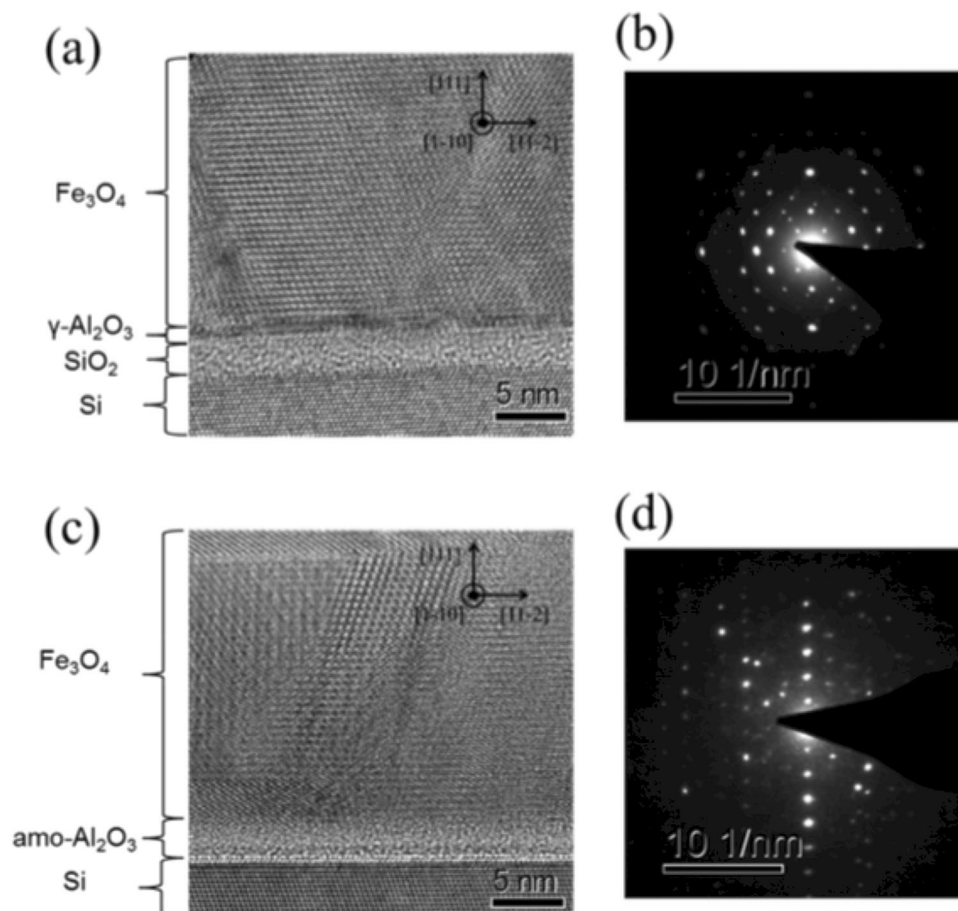


Figure 4. TEM observation: (a) Cross-section TEM image and (b) electron diffraction pattern of Si(111)/ γ -Al₂O₃/Fe₃O₄ in EPI taken along the [1-10] axis zone, (c) Cross-section TEM image and (d) electron diffraction of Si(111)/amo-Al₂O₃/Fe₃O₄ in AMO taken along the [1-10] axis zone.

and amo-SiO. The second possibility is that the amo-Al₂O₃ maintains a crystal structure of Si locally because the amo-Al₂O₃ layer was very thin. Fe₃O₄ could utilize such a microcrystal-like region as a growth nucleus.

Transmission electron microscope observation. We conducted cross-sectional transition electron microscopy (TEM) analysis to confirm the crystallinity and compositions of the materials. Figure 4 shows the cross-section TEM images in which the electron beams were incident along the Si [1-10] zone axis. In Fig. 4(a), the TEM image shows that the Fe atoms of Fe₃O₄ were orderly aligned; thus, the Fe₃O₄ film was epitaxial. The electron diffraction (ED) of Fe₃O₄ in EPI shown in Fig. 4(b) was in good agreement with the simulation of spinel structure. The left side in Fig. 4(a) shows the epitaxial relationship on [11-2]Fe₃O₄(111)/[11-2]Si(111), whereas the center of image shows the epitaxial relationship on [-1-12]Fe₃O₄(111)/[11-2]Si(111), which were consistent with the results of the ϕ -scan measurements in the XRD. In addition, the spacing of the (111) planes were estimated at 4.87 Å from the high angle annular dark-field scanning (HAADF) image (Supplementary Fig. S4(c)), which were almost the same as the out-of-plane lattice constant (4.84 Å) determined by XRD in Fig. 3(a) and that of bulk Fe₃O₄ (4.85 Å). In contrast, the TEM image of Fe₃O₄ in AMO shown in Fig. 4(c) demonstrated that the structure was polycrystalline and grain boundaries were clearly observed. The ED image in Fig. 4(d) consisted of the diffraction from the grains with some crystal orientations. In the low magnification TEM image (supplementary Fig. S4(b)), some grains with a size of 15–30 nm appeared.

With respect to the buffer layer, the thickness of γ -Al₂O₃ was estimated from the HRTEM image (Fig. 4(a)) to be approximately 1 nm, which was thinner than the nominal value measured by the crystal oscillator in the chamber. The reason for this difference in thickness was unclear; however, it could be due to the fluctuation of the crystal oscillator or re-evaporation of Al₂O₃ because the γ -Al₂O₃ was grown at a high temperature (900 °C). We could see the amorphous layer under the γ -Al₂O₃ layer, which was determined to be a SiO_x layer by HAADF and Energy dispersive X-ray spectroscopy (EDS) mapping images (Fig. 5). The SiO_x layer was considered to form during the growth of Fe₃O₄ because the Fe₃O₄ was grown in 4×10^{-4} Pa O₂ gas. It was reported that Si was oxidized through the γ -Al₂O₃ layer of less than 2.0 nm by introducing oxygen ($>10^{-3}$ Pa)³². To confirm that, we fabricated a γ -Al₂O₃ (7.5 nm) film on Si(111), and carried out XRD and TEM observations (supplementary Fig. S5(a) and (b)). The γ -Al₂O₃ grew epitaxially on Si and we found no amorphous layer at the Si(111)/ γ -Al₂O₃(7.5 nm) interface.

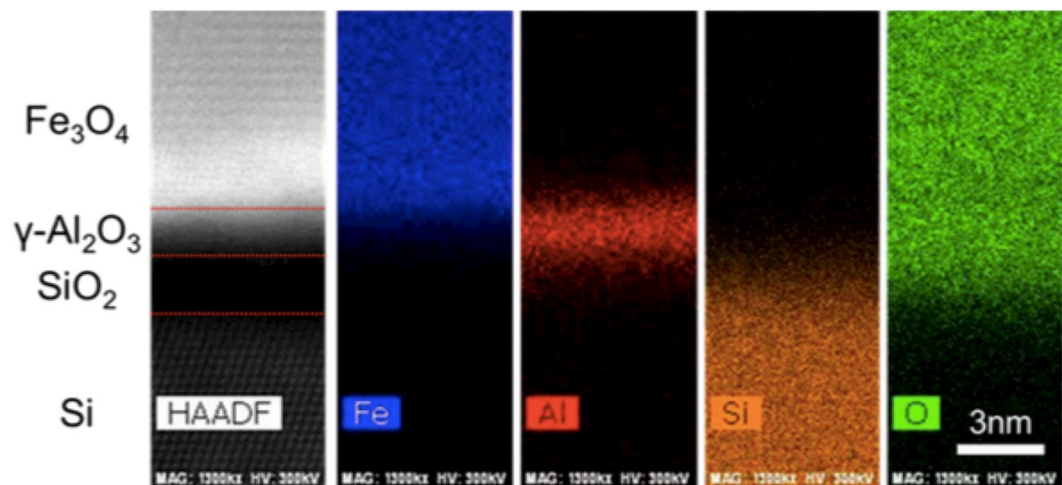


Figure 5. The EDS mapping of the heterostructure: From the left image, HAADF image, EDS mapping of Fe, Al, Si, and O.

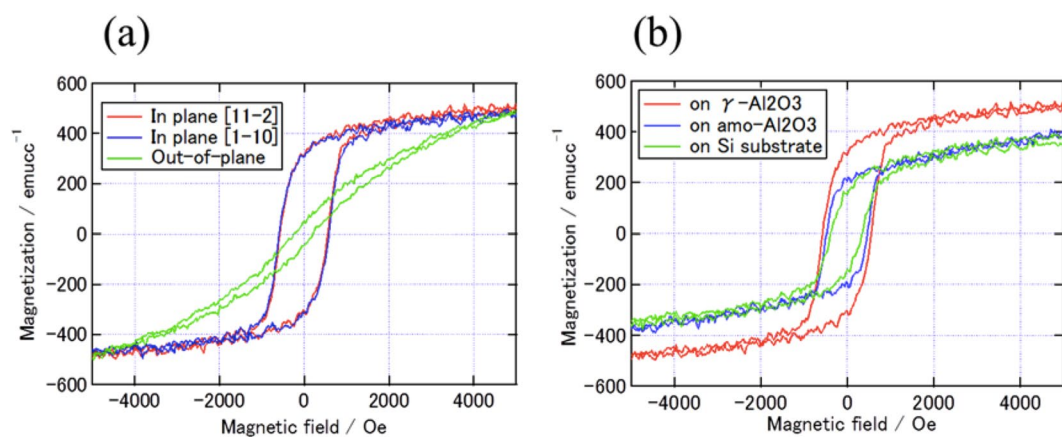


Figure 6. Magnetic properties (a) Magnetization curves of Fe_3O_4 on $\gamma\text{-Al}_2\text{O}_3$ in the magnetic field along [11-2], [1-10], and out of plane [111] (b) Magnetization curves of EPI, AMO, and W/O in the magnetic field along [11-2].

Magnetic characteristics. The magnetic character of Fe_3O_4 is one of its fundamental properties. The magnetization curves at room temperature for the Fe_3O_4 films on $\gamma\text{-Al}_2\text{O}_3$ layer are shown in Fig. 6(a). The directions of the magnetic field were in-plane [11-2], in-plane [1-10] and out-of-plane [111]. The hysteresis curve along [11-2] was the same as that along [1-10] and the Fe_3O_4 film had in-plane magnetization. The saturation magnetization (M_s) was 480 emu/cm^3 for all magnetic field directions. The remanent magnetization (M_r), the coercive field (H_c), and the remanent ratio (M_r/M_s) in the in-plane field were 280 emu/cm^3 , 500 Oe , and 0.48 , respectively, and those for the out-of-plane field were 47 emu/cm^3 , 225 Oe , and 0.08 , respectively. The hysteresis loops for Fe_3O_4 in EPI, AMO, and W/O are illustrated in Fig. 6(b). Fe_3O_4 in EPI had the largest H_c and M_s among the three samples. The M_s of Fe_3O_4 in EPI was the same as the value of bulk Fe_3O_4 . Although the reason for small magnetization for AMO and W/O has not been clear so far, the antiphase boundary or disordered structure at grain boundary could be responsible for it^{33,34}.

Transport characteristics. Figure 7 shows that the dependence of the resistance on temperature for the Fe_3O_4 film in EPI. As is well-known, Fe_3O_4 is an electric conductor at room temperature and the resistivity increases exponentially with decreasing temperature. The resistivity of the film at 300 K was $2.5 \times 10^{-4} \Omega\text{cm}$, which is lower than the bulk value ($5 \times 10^{-3} \Omega\text{cm}$)³⁵. The $\text{dlog}R/\text{d}T$ plots (inset) show a valley at approximately 120 K . This anomaly corresponds to a Verwey transition³⁶, which is a famous phase transition in Fe_3O_4 . The Verwey transition has been reported to sharply change the resistivity by approximately one digit³⁷; however, the transition is easily disappeared by impurities or structure defects^{34,38}. As the Fe_3O_4 in EPI possessed magnetic and electric characteristics that were comparable to bulk Fe_3O_4 , the Fe_3O_4 on $\gamma\text{-Al}_2\text{O}_3$ buffer layer was very good quality.

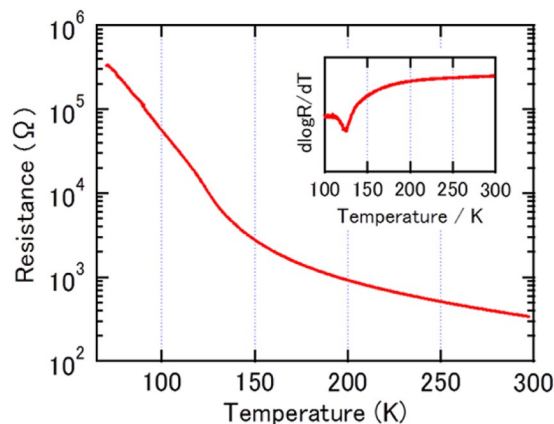


Figure 7. Transport properties: The resistivity of Si(111)/ γ -Al₂O₃/Fe₃O₄ as a function of temperature. The inset is $d\log R/dT$ plot.

Conclusions

We fabricated an epitaxial Fe₃O₄ film on a Si substrate by inserting an γ -Al₂O₃ buffer layer. From the XRD measurement and TEM observation, the γ -Al₂O₃ buffer layer contributed to the growth of epitaxial Fe₃O₄(111) on Si(111). In contrast, the Fe₃O₄ film on an amorphous-Al₂O₃ buffer layer had an (111)-orientation with a textured structure. The Fe₃O₄ on γ -Al₂O₃ had magnetic properties corresponding to the bulk Fe₃O₄, furthermore the resistivity exhibited a Verwey transition at 120 K. The results indicate that the heterostructure of Si substrate/ γ -Al₂O₃/Fe₃O₄ could be used as a part of magnetic tunnel junctions or spin injection devices and will allow us to integrate spintronic devices including Fe₃O₄ electrode, e.g., spin-FET or magnetic tunnel junctions, on Si.

Methods

Preparation of the samples. Before deposition, the Si substrate was cleaned by a standard Radio Corporation of America clean³⁹ and hydrofluoric (HF) acid solution and annealed at 900 °C under a vacuum of $< 10^{-6}$ Pa^[29]. The γ -Al₂O₃ buffer layer was formed by evaporating the Al₂O₃ source material at 900 °C and annealing at 900 °C for 30 minutes. In previous reports, γ -Al₂O₃ was grown at > 850 °C and under a vacuum of $< 10^{-6}$ Pa^[40]. The growth conditions we used for γ -Al₂O₃ were in the range of the report. In Si(111)/amorphous-Al₂O₃/Fe₃O₄, the amorphous-Al₂O₃ was grown at room temperature under a vacuum of $< 3 \times 10^{-6}$ Pa. Then, the Fe₃O₄ film was formed by reactive deposition at 300 °C under a O₂ atmosphere of 4.0×10^{-4} Pa^[41]. All the samples were fabricated under the same growth conditions to investigate the dependence of the quality of Fe₃O₄ films on the buffer layer.

Measurements. The epitaxial growth and crystal structure were confirmed by RHEED, XRD (Rigaku SmartLab (9 kW)), and TEM (FEI Titan3 G2 60-300). Cross-sectional samples for TEM were prepared by using conventional mechanical polishing and dimpling techniques^[42]. The magnetic properties of Fe₃O₄ were measured by vibrating sample magnetometer (VSM) and the electrical properties were measured by direct current (DC) measurements.

References

- Jedema, F. J., Heersche, H. B., Filip, A. T., Baselmans, J. J. A. & van Wees, B. J. Electrical detection of spin precession in a metallic mesoscopic spin valve. *Nature* **416**, 713–716 (2002).
- van't Erve, O. M. J. *et al.* Electrical injection and detection of spin-polarized carriers in silicon in a lateral transport geometry. *Appl. Phys. Lett.* **91**, 212109 (2007).
- Dash, S. J., Sharma, S., Patel, R. S., de Jong, M. P. & Jansen, R. Electrical creation of spin polarization in silicon at room temperature. *Nature* **462**, 491–494 (2009).
- Datta, S. & Das, B. Electronic analog of the electro-optic modulator. *Appl. Phys. Lett.* **56**, 665 (1990).
- Sugahara, S. & Tanaka, M. A spin metal–oxide–semiconductor field-effect transistor using half-metallic-ferromagnet contacts for the source and drain. *Appl. Phys. Lett.* **84**, 2307 (2004).
- Sasaki, T. *et al.* Electrical Spin Injection into Silicon Using MgO Tunnel Barrier. *Appl. Phys. Exp.* **2**, 053003 (2009).
- Johnson, M. & Silsbee, R. H. Interfacial charge-spin coupling: Injection and detection of spin magnetization in metals. *Phys. Rev. Lett.* **55**, 1790 (1985).
- Sasaki, T. *et al.* Spin Transport in Nondegenerate Si with a Spin MOSFET Structure at Room Temperature. *Phys. Rev. Applied* **2**, 034005 (2014).
- Ohishi, M. *et al.* Spin Injection into a Graphene Thin Film at Room Temperature. *Jpn. J. Appl. Phys.* **46**, L605–L607 (2007).
- Shiraishi, M. *et al.* Robustness of Spin Polarization in Graphene-Based Spin Valves. *Adv. Funct. Mater.* **19**, 3711 (2009).
- Bibes, M. & Barthélémy, A. Oxide spintronics. *IEEE Trans. Electron Devices* **54**, 1003 (2007).
- Yanagihara, H., Utsumi, Y., Niizeki, T., Inoue, J. & Kita, E. Perpendicular magnetic anisotropy in epitaxially strained cobalt-ferrite (001) thin films. *J. Appl. Phys.* **115**, 17A719 (2014).
- Takaobushi, J., Kanki, T., Kawai, T. & Tanaka, H. Preparation of ferroelectric field effect transistor based on sustainable strongly correlated (Fe,Zn)₃O₄ oxide semiconductor and their electrical transport properties. *Appl. Phys. Lett.* **98**, 102506 (2011).
- Niizeki, T. *et al.* Observation of longitudinal spin-Seebeck effect in cobalt-ferrite epitaxial thin films. *AIP Advances* **5**, 053603 (2015).
- Yanase, A. & Shiratori, K. Band Structure in the High Temperature Phase of Fe₃O₄. *J. Phys. Soc. Jpn.* **53**, 312 (1984).
- Ramos, A. V. *et al.* Room temperature spin filtering in epitaxial cobalt-ferrite tunnel barriers. *Appl. Phys. Lett.* **91**, 122107 (2007).
- Santos, T. S. & Moodera, J. S. Observation of spin filtering with a ferromagnetic EuO tunnel barrier. *Phys. Rev. B* **69**, 241203 (2004).
- Takahashi, Y. K. *et al.* High spin-filter efficiency in a Co ferrite fabricated by a thermal oxidation. *Appl. Phys. Lett.* **96**, 072512 (2010).

19. Li, P. *et al.* Ultrathin Epitaxial Ferromagnetic γ -Fe₂O₃ Layer as High Efficiency Spin Filtering Materials for Spintronics Device Based on Semiconductors. *Adv. Funct. Mater.* **26**, 5679–5689 (2016).
20. Li, P. *et al.* Spin Filtering in Epitaxial Spinel Films with Nanoscale Phase Separation. *ACS Nano* **11**, 5011–5019 (2017).
21. Ziese, M., Köhler, U., Bollero, A., Höhne, R. & Esquinazi, P. Schottky barrier and spin polarization at the Fe₃O₄-Nb:SrTiO₃ interface. *Phys. Rev. B* **71**, 180406R (2005).
22. Watanabe, H., Fujita, K. & Ichikawa, M. Thermal decomposition of ultrathin oxide layers on Si(111) surfaces mediated by surface Si transport. *Appl. Phys. Lett.* **70**, 1095 (1997).
23. Senn, M. S., Wright, J. P. & Attfield, J. P. Charge order and three-site distortions in the Verwey structure of magnetite. *Nature* **481**, 173–176 (2012).
24. Mi, W., Guo, Z., Wang, Q., Yang, Y. & Bai, H. Charge ordering in reactive sputtered (100) and (111) oriented epitaxial Fe₃O₄ films. *Scripta Materialia* **68**, 972–975 (2013).
25. Liu, X., Yin, L. & Mi, W. Biaxial strain effect induced electronic structure alternation and trimeron recombination in Fe₃O₄. *Sci. Rep.* **7**, 43403 (2017).
26. Dedkov, Y. S., Rüdiger, U. & Güntherodt, G. Evidence for the half-metallic ferromagnetic state of Fe₃O₄ by spin-resolved photoelectron spectroscopy. *Phys. Rev. B* **65**, 064417 (2002).
27. Merckling, C. *et al.* Growth of crystalline γ -Al₂O₃ on Si by molecular beam epitaxy: Influence of the substrate orientation. *J. Appl. Phys.* **102**, 024101 (2007).
28. Jung, Y. C., Miura, H. & Ishida, M. Formation of Very Thin Epitaxial Al₂O₃ Pre-layer with Very Smooth Surface on Si (111) Using a Protective Oxide Layer. *Jpn. J. Appl. Phys.* **38**, 2333 (1999).
29. Merckling, C. *et al.* Epitaxial growth and relaxation of γ -Al₂O₃ on silicon. *Thin Solid Films* **515**, 6479–6483 (2007).
30. Park, C. *et al.* Interfacial composition and microstructure of Fe₃O₄ magnetic tunnel junctions. *IEEE Trans. Magn.* **39**, 2806 (2003).
31. Shirsath, S. E., Liu, X., Yasukawa, Y., Li, S. & Morisako, A. Switching of magnetic easy-axis using crystal orientation for large perpendicular coercivity in CoFe₂O₄ thin film. *Sci. Rep.* **6**, 30074 (2016).
32. Bachelet, R. *et al.* Functional spinel oxide heterostructures on silicon. *Cryst. Eng. Comm.* **16**, 10741–10745 (2014).
33. Margulies, D. T. *et al.* Origin of the Anomalous Magnetic Behavior in Single Crystal Fe₃O₄ Films. *Phys. Rev. Lett.* **79**, 5162 (1997).
34. Mi, W. B., Shen, J. J., Jiang, E. Y. & Bai, H. L. Microstructure, magnetic and magneto-transport properties of polycrystalline Fe₃O₄ films. *Acta Materialia* **55**, 1919–1926 (2007).
35. Eerenstein, W., Palsra, T. T., Hibma, T. & Celotto, S. Origin of the increased resistivity in epitaxial Fe₃O₄ films. *Phys. Rev. B* **66**, 201101(R) (2002).
36. Verwey, E. J. W. Electronic Conduction of Magnetite (Fe₃O₄) and its Transition Point at Low Temperatures. *Nature* **144**, 327–328 (1939).
37. Kado, T., Saito, H. & Ando, K. Room-temperature magnetoresistance in magnetic tunnel junctions with Fe₃O₄ electrode. *J. Appl. Phys.* **101**, 09J511 (2007).
38. Tsuda, N. *et al.* *Electronic Conduction in Oxide* (Springer, Berlin-Heidelberg, 2000)
39. Kern, W. & Puotinen, D. Cleaning solutions based on hydrogen peroxide for use in silicon semiconductor technology. *RCA Review* **31**, 187–206 (1970).
40. Wu, S. Y. *et al.* High-quality thin single-crystal γ -Al₂O₃ films grown on Si(111). *Appl. Phys. Lett.* **87**, 091908 (2005).
41. Nagahama, T. *et al.* Magnetic properties of epitaxial Fe₃O₄ films with various crystal orientations and tunnel magnetoresistance effect at room temperature. *Appl. Phys. Lett.* **105**, 102410 (2014).
42. Lari, L., Lea, S., Feeser, C., Wessels, B. W. & Lazarov, V. K. Ferromagnetic InMnSb multi-phase films study by aberration-corrected (scanning) transmission electron microscopy. *J. Appl. Phys.* **111**, 07C311 (2012).

Acknowledgements

We would like to express our gratitude to Prof. Yamamoto's group, Prof. Tokeshi's group for their cooperation in the microfabrication. We especially thank Prof. Sakaguchi for his advice and helpful suggestions. This work was partly supported by JSPS KAKENHI Grant Numbers 15H05702, 23686006, the Collaborative Research Program of Institute for Chemical Research, Kyoto University (grant 2016-57), and the OPEN FACILITY, Hokkaido University Sousei Hall and Nanotechnology Collaborative Research in Hokkaido University. TH and AH are supported by EU-FP7 HARFIR project (NMP3-SL-2013-604398).

Author Contributions

N.T. and T.N. conceived and designed the experiments using the help of other authors. N.T., T.N., Y.Y., T.Y. and T.S. performed the sample preparation, XRD measurements, magnetic and electrical measurements. T.H., A.H., N.T. and T.N. performed TEM observations. All the authors contributed to analysing and interpreting the data, and to writing the manuscript.

Additional Information

Supplementary information accompanies this paper at doi:10.1038/s41598-017-07104-z

Competing Interests: The authors declare that they have no competing interests.

Publisher's note: Springer Nature remains neutral with regard to jurisdictional claims in published maps and institutional affiliations.



Open Access This article is licensed under a Creative Commons Attribution 4.0 International License, which permits use, sharing, adaptation, distribution and reproduction in any medium or format, as long as you give appropriate credit to the original author(s) and the source, provide a link to the Creative Commons license, and indicate if changes were made. The images or other third party material in this article are included in the article's Creative Commons license, unless indicated otherwise in a credit line to the material. If material is not included in the article's Creative Commons license and your intended use is not permitted by statutory regulation or exceeds the permitted use, you will need to obtain permission directly from the copyright holder. To view a copy of this license, visit <http://creativecommons.org/licenses/by/4.0/>.

© The Author(s) 2017